Title

Electronic interactions in Dirac fluids visualized by nano-terahertz spacetime interference of electron-photon quasiparticles.

Journal

Science Advances, 10(43)

Authors

Xu, Suheng

Li, Yutao

Vitalone, Rocco

et al.

Publication Date

2024-10-25

DOI

10.1126/sciadv.ado5553

Peer reviewed

PHYSICS

Electronic interactions in Dirac fluids visualized by nano-terahertz spacetime interference of electron-photon quasiparticles

Suheng Xu[1]†, Yutao Li[1,2]†, Rocco A. Vitalone[1], Ran Jing[1,3,4], Aaron J. Sternbach[1,5], Shuai Zhang[1], Julian Ingham[1], Milan Delor[6], James W. McIver[1], Matthew Yankowitz[7,8], Raquel Queiroz[1], Andrew J. Millis[1,9], Michael M. Fogler[10], Cory R. Dean[1], Abhay N. Pasupathy[1], James Hone[11], Mengkun Liu[3,12], D. N. Basov[1]*

Ultraclean graphene at charge neutrality hosts a quantum critical Dirac fluid of interacting electrons and holes. Interactions profoundly affect the charge dynamics of graphene, which is encoded in the properties of its electron-photon collective modes: surface plasmon polaritons (SPPs). Here, we show that polaritonic interference patterns are particularly well suited to unveil the interactions in Dirac fluids by tracking polaritonic interference in time at temporal scales commensurate with the electronic scattering. Spacetime SPP interference patterns recorded in terahertz (THz) frequency range provided unobstructed readouts of the group velocity and lifetime of polariton that can be directly mapped onto the electronic spectral weight and the relaxation rate. Our data uncovered prominent departures of the electron dynamics from the predictions of the conventional Fermi-liquid theory. The deviations are particularly strong when the densities of electrons and holes are approximately equal. The proposed spacetime imaging methodology can be broadly applied to probe the electrodynamics of quantum materials.

INTRODUCTION

Plasmon polaritons are coherent electron density oscillations dressed with electromagnetic fields. These collective modes play a prominent role in the charge response of metals and semiconductors. Graphene is an exemplary platform for plasmonics due to its high tunability and relatively low electronic losses (*1*–*4*). In most previous studies of plasmon polaritons in graphene, the graphene was heavily doped, so that many-body effects did not qualitatively alter the conventional Fermi-liquid picture of charge dynamics (*3*). However, electrons in graphene near the charge neutral point (CNP) form a correlated Dirac fluid (*5*–*7*), which exhibits unusual behaviors such as a quantum critical scattering rate, breakdown of Wiedemann-Franz law, and large magnetoresistance (*8*–*12*). These exotic properties stem from electron-electron interactions, whose strength is parametrized by the ratio between Coulomb energy and kinetic potential: the effective fine-structure constant $\alpha = e^2/\epsilon\hbar v_F$ (*13*–*15*). Here, ϵ is the dielectric constant of the environment, and v_F is the graphene Fermi velocity.

To investigate the collective behavior of the Dirac fluid, we visualized the "worldlines" of surface plasmon polaritons (SPPs), i.e., the trajectories of polaritonic wave packets in spacetime. The experiments were performed using a home-built cryogenic terahertz scanning near-field optical microscope (THz-SNOM) (*16*–*18*) that gave us access to subpicosecond dynamics with sub-50-nm spatial resolution. From the measured SPP worldlines, we extracted two key observables, the SPP group velocity v_g and the SPP lifetime τ_p, that provided evidence for non–Fermi-liquid effects in the charge dynamics.

[1]Department of Physics, Columbia University, New York, NY 10027, USA. [2]Brookhaven National Laboratory, Upton, NY 11973, USA. [3]Department of Physics and Astronomy, Stony Brook University, Stony Brook, NY 11794, USA. [4]Condensed Matter Physics and Materials Science Department, Brookhaven National Laboratory, Upton, NY 11973, USA. [5]Department of Physics, University of Maryland, College Park, MD 20742, USA. [6]Department of Chemistry, Columbia University, New York, NY 10027, USA. [7]Department of Physics, University of Washington, Seattle, WA 98195, USA. [8]Department of Materials Science and Engineering, University of Washington, Seattle, WA 98195, USA. [9]Center for Computational Quantum Physics, The Flatiron Institute, 162 5th Avenue, New York, NY 10010, USA. [10]Department of Physics, University of California at San Diego, La Jolla, CA 92093, USA. [11]Department of Mechanical Engineering, Columbia University, New York, NY 10027, USA. [12]National Synchrotron Light Source II, Brookhaven National Laboratory, Upton, NY 11973, USA.
*Corresponding author. Email: db3056@columbia.edu
†These authors contributed equally to this work.

RESULTS

Nano-THz response of a graphene ribbon

We investigated graphene ribbons encapsulated in hexagonal boron nitride (hBN). The ribbons were integrated in a back-gated structure assembled on a Si/SiO_2 wafer. Ohmic Cr/Au contacts enabled electrical measurements (Fig. 1A; see Materials and Methods and text S1). Our THz-SNOM operated with broadband THz pulses, spanning a range of frequencies from 0.5 to 1.5 THz (Fig. 1A), generated via a photo-conductive antenna (PCA). The THz pulses were focused on the tip of an atomic force microscope, and the forward-scattered THz pulses were detected by another PCA with subpicosecond temporal resolution. The demodulation of the detected signal produced artifact-free THz images with a 50-nm spatial resolution as described in (*16*, *17*) (see Materials and Methods). By raster scanning the sample under the tip, we obtained images of the amplitude and phase of the local THz electric field (*18*).

A representative image of a nano-THz signal is shown in Fig. 1B. The false color plot displays the amplitude of the local field. The nano-THz signal on graphene is enhanced compared to that of the substrate owing to the higher THz conductivity. The nano-THz response is maximized at the center of the graphene ribbon. This spatially inhomogeneous response originates from the graphene SPP, as we detail below. To help us analyze the data, we calculated the THz near-field reflection coefficient (r_p) for our structure, which is composed of encapsulated graphene, 285-nm-thick SiO_2, and the Si back gate. (Fig. 1C). The SPP dispersion manifests itself as a line of enhanced Im r_p (*19*) in the frequency-momentum parameter space (the red dashed line in

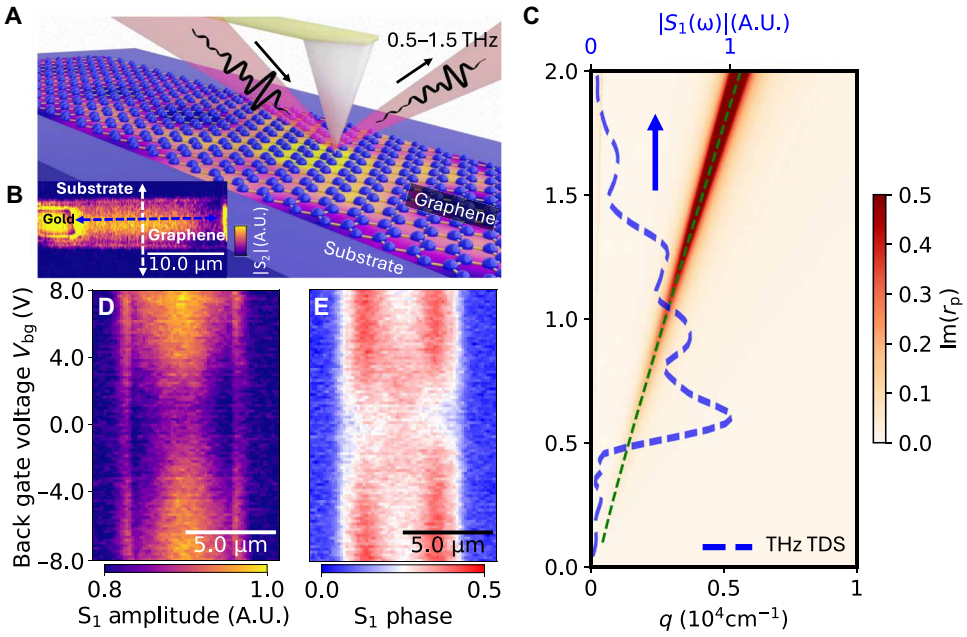

Fig. 1. Nano-THz imaging of plasmons in a gateable graphene cavity. (**A**) Schematics of the nano-THz experiment setup. A monolayer graphene ribbon encapsulated by hBN resides on a SiO_2/Si substrate and is illuminated with broadband THz pulses (0.5 to 1.5 THz). The tip acts as a nano-antenna, launching and detecting polaritonic wave packets. (**B**) Nano-THz image of the broadband THz signal on a graphene ribbon at V_{bg}=5 V and T = 297 K. (**C**) The imaginary part of the reflection coefficient (r_p) calculated as a function of momentum and frequency at carrier density $n = 1.1 \times 10^{12}$ cm^{-2}. The maximum of Im(r_p), indicated by the green dashed line, traces the SPP dispersion, which is nearly linear in momentum. The spectrum of the nano-THz pulse is plotted as a blue dashed line. (**D** and **E**) Gate voltage dependence of nano-THz amplitude and phase profile across the graphene ribbon, obtained by scanning along the white dashed line marked in (B). A.U., arbitrary units.

Fig. 1C). The nearly linear (rather than common square root–like) dispersion of the graphene SPP in the parameter space accessible with THz nano-imaging is caused by the screening from the back gate (text S2).

To complete the basic nano-THz characterization of our structure, we investigated the evolution of the response of graphene as we tuned its Fermi level with the gate voltage V_{bg}. In Fig. 1 (D and E), we show data obtained by scanning across the graphene ribbon (along the dashed line in Fig. 1B) while varying V_{bg}. The amplitude of the nano-THz signal increases with the gate voltage as the Fermi level is driven away from the CNP and the graphene THz conductivity increases (*20*). The CNP of the sample is at $V_{bg} \sim 0$ V, attested by the symmetric gate dependence in Fig. 1 (D and E) and further confirmed by transport measurements (text S3). At low carrier densities ($|V_{bg}| < 3$ V), both the amplitude and phase of the nano-THz signal are maximized at the center of the ribbon. However, at $|V_{bg}| > 3$ V, the maximum of the phase signal shifts to the edges, whereas the amplitude signal remains most prominent at the center. These observations can be explained by the change in the SPP wavelength (*18*) (text S7): Namely, our sample acts as a plasmonic cavity supporting multiple reflections at the ribbon boundaries, which create wavelength-dependent interference patterns in the interior of the cavity. As we sweep the back gate voltage from $|V_{bg}| = 0$ V to $|V_{bg}| = 30$ V, the calculated wavelength of THz SPPs grows from 5 to 26 μm, the latter number exceeding the width of the ribbon.

Spacetime mapping of electron-photon polaritons

Tracking the moving polaritonic wave packets necessitates high spatial and temporal resolution. For example, the spatiotemporal dynamics of infrared hyperbolic phonon polariton in hBN was visualized by ultrafast transmission electron microscopes and scattering-type SNOMs (s-SNOM) integrated with time-domain interferometry (*21*, *22*). THz waves traveling in graphene metamaterials have also been visualized using aperture-based THz near-field probe and spatially resolved electro-optical sampling, achieving a spatial resolution of a few micrometers (*23*, *24*). Inspired by these innovations, we devised and implemented nano-THz spacetime imaging offering a direct access to the electric field profiles of polariton wave packets with the spatial resolution down to 10^{-4} of the THz wavelengths in free space.

Here, we used our THz-SNOM, which incorporates the THz time-domain spectroscopy(thz-tds) and s-SNOM and simultaneously offers exceptional spatial and temporal resolution to record the SPP dynamics in graphene on a map with ultrafine spacetime pixel. A representative map collected at $V_{bg} = 15$ V and $T = 297$ K is presented in Fig. 2B. To obtain this map, we scanned the tip along the white dashed line in Fig. 1B while slowly varying the time delay, thus unfolding the temporal profile of the scattered THz pulses (text S4). The signal along the vertical time axis manifests itself as a time-domain trace of the tip-scattered THz pulse. One typical trace shown in Fig. 2A is extracted from the center of the graphene ribbon (black dashed line in Fig. 2B). To eliminate the spatially uniform background, we applied the second spatial derivative to this spacetime map. As shown in Fig. 2C (also text S5), the derivative plot reveals a periodic checkerboard pattern.

The formation of the checkerboard pattern can be understood from the geometrical construction shown in Fig. 2D. Consider an SPP launching event at $t = 0$ ps by the tip located at a distance x_1 from the edge. Since the SPP dispersion is almost linear (Fig. 1E), various frequency components of the broadband THz pulse create polaritons propagating with the same speed v_g. The launched SPP

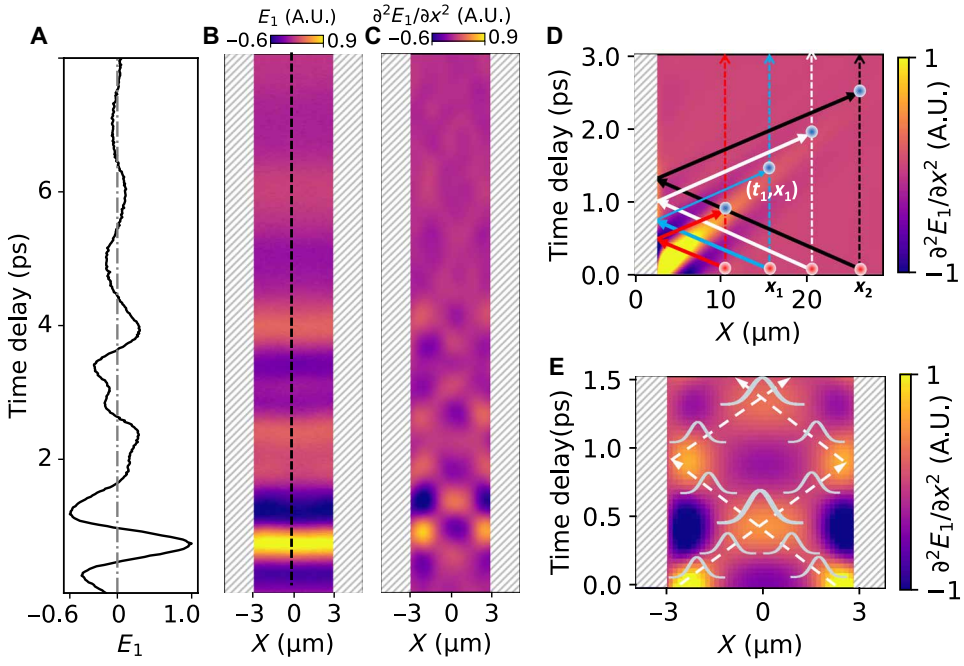

Fig. 2. Spacetime mapping of plasmon polaritons in a graphene ribbon cavity. (**A**) THz time-domain signal collected with the tip located at the center of the graphene ribbon. (**B**) Nano-THz spacetime map. The data are obtained by scanning the tip along the same line across the graphene sample while sweeping the time delay between the scattered THz pulse and the optical detection beam. The substrate region is indicated by the gray shaded area. (**C**) Second spatial derivative of the data in (B), showing the checkerboard pattern. This pattern is generated by SPP wave packets launched by the tip as they propagate across the ribbon and reflect off its edges. (**D**) Simulated spacetime map in a half-plane sample where SPPs are launched at a time delay of 0 ps by the tip, located at various distances *X* from the edge. The launching events are labeled with the red dots and the detection events with the blue dots. The solid arrows whose slope is equal to the reciprocal of the SPP group velocity show the plasmon trajectories. The coalescence of detection event traces forms the worldline of the SPPs. In these numerical simulations, the group velocity is 20 μm/ps and the plasmon lifetime is 0.85 ps. (**E**) Simulated nano-THz spacetime map of SPPs in a ribbon cavity. The substrate region is marked by the shaded area. The dashed white lines mark the SPP detection worldline.

wave packet travels outward from the tip, undergoes a reflection from the edge, and then travels inward. If the propagation losses are not too large, so that the reflection wave packet is able to complete the round trip, then this event is detected by the THz-SNOM at time $t_1 = 2x_1/v_g$. In Fig. 2D, we depict a few such launching and detection events (red and blue dots) as well as the corresponding round-trip SPP trajectories (solid lines with slopes $\pm v_g^{-1}$). As the tip is moved away from the edge, the detection time grows proportionally longer, producing an SPP "detection worldline" in the spacetime coordinates. This worldline emanates from the point ($x = 0$, $t = 0$) and has slope $2/v_g$. The worldline fades away at large distances and long times, providing information about plasmonic losses. A more comprehensive elucidation of the spacetime map is provided in text S4.

In the above discussion, we considered the SPP reflections only from the edge nearest to the tip. In Fig. 2E, we model the spacetime map for the case of a finite-width plasmonic cavity where both edges can reflect the SPPs, so that each of them generates a worldline (supplemental material S6). The worldlines begin at $t = 0$ at the two opposite edges and tilt inward to intersect at the center. At the intersection point, the SPP wave packets reflected from the two edges return to the tip simultaneously. The worldlines reverse their slope once they reach an edge of the ribbon; this corresponds to repeated reflections of the wave packets inside the cavity. Because of the finite width of the wave packets, the net observable pattern resembles a checkerboard pattern, in agreement with the experimental data in Fig. 2C.

SPP dynamics and worldlines

To study the dynamics of the SPP wave packets, we obtained spacetime maps at various temperatures at a fixed back gate voltage. In Fig. 3 (A to C), we present three spacetime maps collected at $T =$ 300, 170, and 55 K (all at $V_{bg} = 15$ V). In the spacetime maps, the SPPs at lower temperatures show more robust and longer-lived oscillations. The temporal oscillations of the SPPs extracted from the center of the spacetime map [white dashed lines in Fig. 3 (A to C)] are summarized in Fig. 3D. These oscillations can be modeled as described in text S9. The best fit to the experimental data is found when the simulated plasmon lifetime is 0.75, 1.8, and 4.75 ps (Fig. 3D and text S8). These plasmon lifetimes correspond to plasmonic relaxation rates ($1/\tau_p$) of 1.33, 0.56, and 0.21 THz, respectively. Except for the first one, these lifetimes are longer than the previously measured record-high lifetime of infrared SPPs (*3*) [1.6 ps at $T = 60$ K and photon energy of ~110 meV (*3*)].

The spacetime patterns of polaritonic wave packets (Figs. 2 and 3) are ultimately governed by the dispersion of SPP in the frequency (ω)–momentum (q) space. The SPP dispersion can be derived from the pole of the near-field reflection coefficient via $r_p(q, \omega) \simeq 1 - (2qd/\epsilon_{2D})$ for $q \gg \omega/c$. Here, $\epsilon_{2D} = 1 + (iq^2/\omega)e^2V\sigma$ is the two-dimensional (2D) dielectric function of graphene, $V = V(q, \omega)$ is the effective Coulomb interaction kernel, and σ is the sheet conductivity (*25*). Under our experimental conditions, V is well approximated by the inverse capacitance $V = C^{-1} = 4\pi d/\epsilon$ per unit area, where d is the distance between the graphene and the gate and ϵ is the dielectric

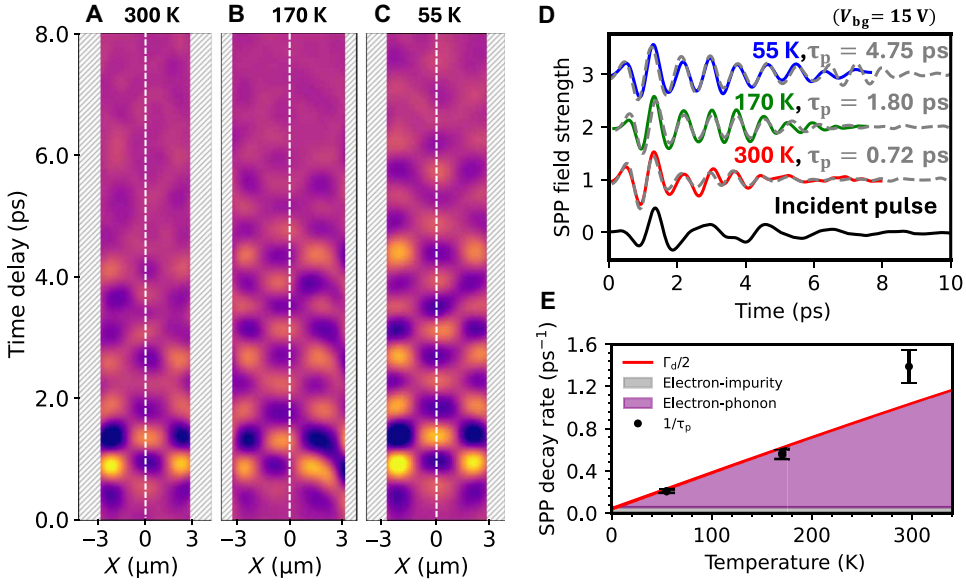

Fig. 3. Temperature dependence of the SPP relaxation rate in the Fermi-liquid regime. (**A** to **C**) Second-order spatial derivatives of spacetime maps taken at 300, 170, and 55 K, all at gate voltage V_g = 15 V. (**D**) Temporal oscillations of the SPP field at the center of the graphene cavity along the white dashed lines in (A) to (C). The gray dashed lines are simulated temporal oscillations yielding the SPP lifetimes of 0.75 ps (T = 300 K), 1.8 ps (T = 170 K), and 4.75 ps (T = 55 K). The black solid line is the THz scattering signal probed at the location of the gold launcher. (**E**) Temperature dependence of the SPP decay rate (inverse lifetime). The black dots are the SPP decay rates $1/\tau_p$ extracted from the fittings in (D). The red curve is the estimate of the SPP relaxation rate, considering various momentum-relaxing scattering mechanisms as described in the text. The gray shaded region shows the relaxation rate contributed by electron-impurity scattering, whereas the magenta region depicts the contribution of electron-phonon scattering. The scattering rate analysis is described in text S10.

constant of the spacer. The nontrivial physics we observe is encoded in the optical conductivity $\sigma = \sigma(\omega)$, accessible through the analysis of SPP worldlines and dispersions.

In the Fermi-liquid regime realized in heavily doped graphene with the chemical potential μ exceeding the temperature $\mu \gg k_bT$, the conductivity is well captured by the Drude formula

$$\sigma(\omega) = \frac{i}{\pi}\frac{D}{\omega + i\Gamma_d} \quad (1)$$

where D is the Drude weight and Γ_d is the momentum-relaxing scattering rate (*26*). Assuming $\omega \gg \Gamma_d$, the corresponding observables in spacetime maps read as

$$v_g = \sqrt{\frac{D}{\pi C}}, \tau_p = \frac{2}{\Gamma_d} \quad (2)$$

The SPP lifetime (τ_p) is twice as large as the invers of Γ_d, which can be attributed to the screening effect produced by the back gate (see Supplemental section S9 for details). Hence, the two main characteristics of the SPP worldlines—the slope ($2/v_g$) and the decay time (τ_p)—are governed in the Drude model by the Drude weight and the scattering rate, respectively. Both quantities can be directly measured as the geometrical metrics of worldlines. The calculated SPP decay rate (red curve in Fig. 3E) shows that a combination of electron-phonon and impurity scattering is in quantitative agreement with the SPP-extracted data, as detailed in text S10.

Electronic interactions from spacetime metrology

We now focus on the SPP spacetime dynamics in the vicinity of the CNP. Our THz spacetime maps collected at ambient temperature reveal plasmonic propagation at gate voltages as low as 5, 1, or even 0 V at the CNP (Fig. 4). We attribute the presence of SPPs at the CNP to the response of thermally excited electrons and holes (*9*, *10*, *27*, *28*). The SPP group velocity increases with gate voltage, as evidenced by shallower worldline slopes [dashed arrows in Fig. 4 (A to C and E to G)]. The evolution of the group velocity as a function of the back gate voltage is summarized in Fig. 4D. The group velocity of SPP increases with carrier density from 6 μm/ps or 2% of the speed of light near the CNP to 26 μm/ps at V_{bg} = 30 V. The worldline of the SPPs at the CNP is short-lived: The plasmonic wave packets cease to exist after only 0.2 to 0.3 ps. Applying a gate voltage as low as 1 V nearly doubles the lifetime manifested by the extended SPP propagation range. We quantify the SPP lifetime by analyzing the temporal decay of the SPP field along the worldlines of SPP that travel along the ribbon at various gate voltages (Fig. 4H, with additional details presented in text S13). The SPP relaxation rate decreases from ~5 THz at the CNP to less than 1.5 THz at μ > 120 meV (Fig. 4I). The significant enhancement of the SPP relaxation rate at the CNP cannot be explained solely by the momentum-relaxing scattering rates, which generally either remain unchanged or decrease with carrier density (*29*). The influence of the interband transition in nano-THz data is also negligible (text S12).

Searching for the origins of the evolution of the SPP dynamics in Fig. 4 (D and I), we recall that in the absence of Umklapp processes, dc charge transport in monopolar Fermi liquids is not impeded by momentum-conserving electron scattering because the total momentum and current are proportional to each other. This is the case in highly doped graphene. However, the situation is different in materials hosting both electrons and holes (*14*, *30*–*32*) such as charge-neutral graphene at a finite temperature. The electron-hole scattering produces current relaxation and therefore enhanced plasmonic losses (*30*, *33*–*35*). Below, we attempt to verify the importance of this

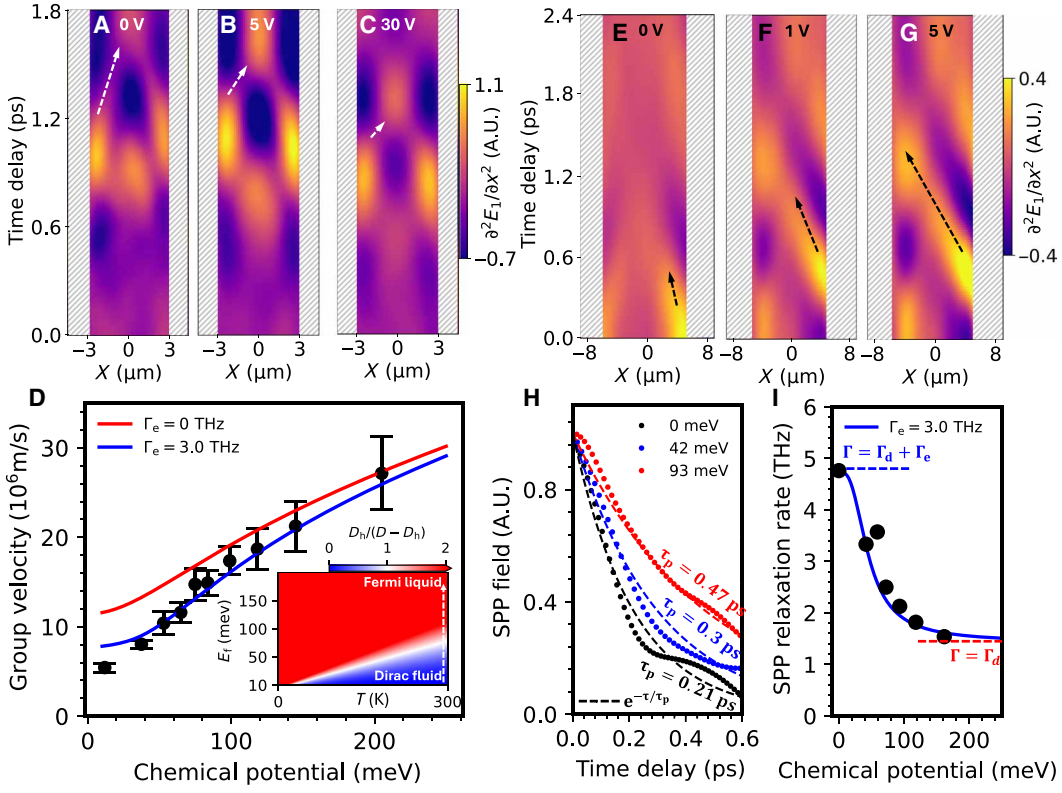

Fig. 4. SPP dynamics renormalized by electronic interactions in Dirac fluid. (**A** to **C**) Spacetime maps collected across the graphene ribbon when applying different back gate voltages. White arrows mark the slopes of the SPP worldline. A shallower slope corresponds to a faster SPP group velocity. (**D**) Dots display the gate dependence of the graphene SPP group velocity at 300 K. Solid red line: theoretical group velocity obtained from Eq. 3 by setting $\Gamma_e = 0$ THz, as described in the text. The solid blue trace was obtained by setting the electronic scattering rate $\Gamma_e = 3$ THz. The false color map in the inset of (D) presents the ratio between the two numerators D_h and $D_k - D_h$ in the two-component model (Eq. 3). The white dashed line presents the trajectory of gate-dependent measurements probing the transition from a Dirac fluid regime to a Fermi-liquid regime. (**E** to **G**) Spacetime maps collected along the graphene ribbon (marked as blue dashed lines in Fig. 1B) at $V_g = 0$ V (E), 1 V (F), and 5 V (G). The black arrows mark the SPP worldlines. (**H**) Time-dependent polariton field strength extracted along the SPP worldlines in (E) to (G). The field strength is normalized by its maximum value. The dashed curves show the exponential decay e^{-t/τ_p} controlled by the SPP lifetime τ_p. (**I**) Dirac-fluid/Fermi-liquid crossover visualized by the gate-dependent SPP relaxation at room temperature. In the Dirac fluid regime ($E_f \ll k_bT$), the SPP damping is determined by $\Gamma_d + \Gamma_e$ (marked by the blue dashed line). In the Fermi-liquid regime ($E_f \gg k_bT$), the SPP damping is solely determined by Γ_d (marked by the red dashed line). The blue solid line shows the calculated gate-dependent SPP relaxation rate based on the two-fluid model ($\Gamma_d = 0.47$ THz, $\Gamma_e = 3$ THz).

so-called electron-hole drag effect by examining how the conductivity we deduce from our measurements varies as a function of the gate voltage at a finite temperature.

For the quantitative analysis of the doping dependence trends in Fig. 4, we have adopted the two-component model of the THz conductivity of graphene (*36*)

$$\sigma_h(\omega) = \frac{i}{\pi}\frac{D_h}{\omega + i\Gamma_d} + \frac{i}{\pi}\frac{D_k - D_h}{\omega + i\Gamma_d + i\Gamma_e} \quad (3)$$

where D_h is the so-called hydrodynamic Drude weight and D_k is the kinetic Drude weight; Γ_d is the momentum-relaxing scattering rate attributed to the combined action of impurities and phonons; and Γ_e is the electronic scattering rate (text S13). The first term in Eq. 3 describes the contribution from the hydrodynamic-type flow, where all the charge carriers move in the same direction. Accordingly, D_h is nonzero only away from the CNP. The second term in Eq. 3 represents the contribution associated with the electrons and holes moving in opposite directions in response to the same electric field. The electron-hole drag is manifest in the added momentum relaxation rate Γ_e of this term. We display the ratio of the spectral weights (i.e., the numerators) of the two contributions in the inset of Fig. 4D. This plot shows that the hydrodynamic Dirac fluid behavior dominates the graphene response at elevated temperatures and at lower carrier densities.

As shown in Fig. 4 (D and I), the two-component model (Eq. 3) captures the trends seen in the evolution of both the scattering rate and the group velocity as functions of the chemical potential . For simplicity, we assumed that the scattering rates Γ_d and Γ_e are constant and obtained the best fit to the data for $\Gamma_e = 3.0$ THz and $\Gamma_d = 0.47$ THz. These choices of parameters reproduce the entire gate-dependent dataset developed from 17 separate spacetime maps. We remark that in a more accurate model, Γ_e should decrease away from the CNP as the system evolves into a liquid with a progressively larger Fermi surface (*37*). At the CNP, the hydrodynamic term in Eq. 3 vanishes, so that the current relaxation rate reaches its maximum value of $\Gamma_d + \Gamma_e$. At the CNP, the electronic scattering time Γ_e^{-1} is actually shorter than a single oscillation cycle of the SPPs, yet the effect is still observable in our data. Simultaneously, the SPP group velocity v_g attains its minimum at the CNP (blue and red lines in Fig. 4D). Evidently, electronic interactions slow down the SPP in a Dirac fluid in a manner analogous to a viscous drag. From the fitted Γ_e, we estimate

the graphene fine-structure constant as 0.34 (text S16), which matches the theoretical estimate (assuming $v_F = 1.3 \times 10^6$m/s and $\kappa = 5$).

DISCUSSION

To summarize, we introduced a nano-THz spacetime metrology to measure the group velocity and lifetime of SPP wave packets in graphene. The developed spacetime mapping method grants access to the low-energy electrodynamics of quantum materials with subdiffraction and subcycle spacetime resolution on the order of 50nm × 50fs. Our observations revealed a significant renormalization of both parameters near the charge neutrality point of graphene, which is consistent with the electron-hole drag effect in the Dirac fluid. Our nano-THz spacetime mapping opens a new realm for spatiotemporal control of polaritons (*21*, *22*, *24*, *38*–*46*) and for nanospectroscopy of low-energy collective modes in many other quantum materials (*47*–*53*).

MATERIALS AND METHODS

Sample fabrication and geometry

Encapsulating graphene with two hBN layers is known to notably improve the carrier mobility of graphene devices (*54*). To fabricate such a device, hBN and graphene flakes are first mechanically exfoliated onto SiO_2/Si wafer chips. Then, using a polypropylene carbonate (PPC) transfer slide, an hBN-graphene-hBN heterostructure is assembled. The top hBN needs to be thin (<10 nm) so that the s-SNOM can effectively probe the electromagnetic response of the graphene underneath. However, thin hBN flakes are difficult to pick up using PPC. To get around this, the topmost hBN is a thick (~30 nm) flake with a thin (~7 nm) appendage. The presence of the thick part of the flake allows for relatively easy pickup by the PPC transfer slide. The graphene and bottom hBN flakes overlap with both the thick and thin parts of the top hBN, although only the area underneath the thin part of hBN is used in the actual device.

The hBN-graphene-hBN stack, residing on the PPC transfer slide, is released onto a Piranha-cleaned SiO_2/doped Si chip with alignment markers at 115°C. During the release process, special care is taken to remove the "bubbles" trapped between the layers of the stack by repeatedly expanding/shrinking the frontier of PPC/stack contact at 80°C. To remove the remaining PPC film, the SiO_2/Si chip is annealed at 360°C, $<10^{-5}$ mbar for 30 min. E-beam lithography is used to define the ribbon shape of the device, with bilayer 495 A4/950 A2 polymethyl methacrylate as the etch mask. Reactive ion etching using CHF_3/Ar and O_2 removes the heterostructure outside the etch mask. After etching, the remaining PPC is dissolved by acetone, leaving the ribbon behind. Last, e-beam lithography and e-beam metal evaporation are used to fabricate a pair of edge contacts to graphene that lead to two 200 μm by 200 μm metal pads. The two pads and the doped Si are connected to pins on the sample holder by gold wires glued with silver paste on both ends.

During the measurement, the graphene is grounded while the doped Si is supplied with a dc bias V_{bg}. On the basis of the parallel capacitor model, the average carrier density in graphene can be determined from V_{bg} and the thickness and permittivity of the dielectric spacer.

THz scanning near-field optical microscopy

We conducted all the THz near-field measurements using the home-built cryogenic THz scanning near-field optical microscope (*16*–*18*). The THz broadband pulse is generated and detected by a pair of PCAs (Menlo Systems GmbH). Our home-built cryogenic ultrahigh vacuum atomic force microscope is operated in the tapping mode, in which the cantilever of a metallic tip (Rocky Mountain Nanotechnology LLC) vibrates near its fundamental resonance frequency (30 to 80 kHz). The THz radiation from the PCA emitter is collimated by a TPX lens and focused onto the tip and sample by a parabolic mirror. The scattered field is detected by an unbiased PCA, and the photocurrent signal is demodulated by a lock-in amplifier at harmonics of the tip tapping frequency. Through this demodulation, we effectively probe the near-field tip-sample interaction with a spatial resolution on the order of 50 nm.

Supplementary Materials

This PDF file includes:

Supplementary Text
Figs. S1 to S15
Table S1
References

REFERENCES AND NOTES

1. D. N. Basov, M. M. Fogler, F. J. G. De. Abajo, Polaritons in van der Waals materials. *Science* **354**, aag1992 (2016).
2. Z. Fei, A. S. Rodin, G. O. Andreev, W. Bao, A. S. McLeod, M. Wagner, L. M. Zhang, Z. Zhao, M. Thiemens, G. Dominguez, M. M. Fogler, A. H. C. Neto, C. N. Lau, F. Keilmann, D. N. Basov, Gate-tuning of graphene plasmons revealed by infrared nano-imaging. *Nature* **487**, 82–85 (2012).
3. G. X. Ni, A. S. McLeod, Z. Sun, L. Wang, L. Xiong, K. W. Post, S. S. Sunku, B.-Y. Jiang, J. Hone, C. R. Dean, M. M. Fogler, D. N. Basov, Fundamental limits to graphene plasmonics. *Nature* **557**, 530–533 (2018).
4. J. Chen, M. Badioli, P. Alonso-González, S. Thongrattanasiri, F. Huth, J. Osmond, M. Spasenović, A. Centeno, A. Pesquera, P. Godignon, A. Z. Elorza, N. Camara, F. J. G. de Abajo, R. Hillenbrand, F. H. L. Koppens, Optical nano-imaging of gate-tunable graphene plasmons. *Nature* **487**, 77–81 (2012).
5. A. Lucas, K. C. Fong, Hydrodynamics of electrons in graphene. *J. Phys. Condens. Matter* **30**, 053001 (2018).
6. A. Lucas, An exotic quantum fluid in graphene. *Science* **364**, 125–125 (2019).
7. M. Polini, A. K. Geim, Viscous electron fluids. *Phys. Today* **73**, 28–34 (2020).
8. P. Gallagher, C.-S. Yang, T. Lyu, F. Tian, R. Kou, H. Zhang, K. Watanabe, T. Taniguchi, F. Wang, Quantum-critical conductivity of the Dirac fluid in graphene. *Science* **364**, 158–162 (2019).
9. W. Zhao, S. Wang, S. Chen, Z. Zhang, K. Watanabe, T. Taniguchi, A. Zettl, F. Wang, Observation of hydrodynamic plasmons and energy waves in graphene. *Nature* **614**, 688–693 (2023).
10. N. Xin, J. Lourembam, P. Kumaravadivel, A. E. Kazantsev, Z. Wu, C. Mullan, J. Barrier, A. A. Geim, I. V. Grigorieva, A. Mishchenko, A. Principi, V. I. Fal'ko, L. A. Ponomarenko, A. K. Geim, A. I. Berdyugin, Giant magnetoresistance of Dirac plasma in high-mobility graphene. *Nature* **616**, 270–274 (2023).
11. J. A. Sulpizio, L. Ella, A. Rozen, J. Birkbeck, D. J. Perello, D. Dutta, M. Ben-Shalom, T. Taniguchi, K. Watanabe, T. Holder, R. Queiroz, A. Principi, A. Stern, T. Scaffidi, A. K. Geim, S. Ilani, Visualizing Poiseuille flow of hydrodynamic electrons. *Nature* **576**, 75–79 (2019).
12. J. Crossno, J. K. Shi, K. Wang, X. Liu, A. Harzheim, A. Lucas, S. Sachdev, P. Kim, T. Taniguchi, K. Watanabe, T. A. Ohki, K. C. Fong, Observation of the Dirac fluid and the breakdown of the Wiedemann-Franz law in graphene. *Science* **351**, 1058–1061 (2016).
13. D. E. Sheehy, J. Schmalian, Quantum critical scaling in graphene. *Phys. Rev. Lett.* **99**, 226803 (2007).
14. L. Fritz, J. Schmalian, M. Müller, S. Sachdev, Quantum critical transport in clean graphene. *Phys Rev. B* **78**, 085416 (2008).
15. V. N. Kotov, B. Uchoa, V. M. Pereira, F. Guinea, A. H. C. Neto, Electron-electron interactions in graphene: Current status and perspectives. *Rev. Mod. Phys.* **84**, 1067–1125 (2012).
16. H. T. Stinson, A. Sternbach, O. Najera, R. Jing, A. S. Mcleod, T. V. Slusar, A. Mueller, L. Anderegg, H. T. Kim, M. Rozenberg, D. N. Basov, Imaging the nanoscale phase separation in vanadium dioxide thin films at terahertz frequencies. *Nat. Commun.* **9**, 3604 (2018).
17. R. Jing, Y. Shao, Z. Fei, C. F. B. Lo, R. A. Vitalone, F. L. Ruta, J. Staunton, W. J.-C. Zheng, A. S. Mcleod, Z. Sun, B. Jiang, X. Chen, M. M. Fogler, A. J. Millis, M. Liu, D. H. Cobden, X. Xu, D. N. Basov, Terahertz response of monolayer and few-layer WTe2 at the nanoscale. *Nat. Commun.* **12**, 5594 (2021).

18. R. Jing, R. A. Vitalone, S. Xu, C. F. B. Lo, Z. Fei, E. Runburg, Y. Shao, X. Chen, F. Mooshammer, A. S. Mcleod, M. Liu, M. M. Fogler, D. H. Cobden, X. Xu, D. N. Basov, Phase-resolved terahertz nanoimaging of WTe_2 microcrystals. *Phys Rev. B* **107**, 155413 (2023).
19. B.-Y. Jiang, L. M. Zhang, A. H. C. Neto, D. N. Basov, M. M. Fogler, Generalized spectral method for near-field optical microscopy. *J. Appl. Phys.* **119**, 054305 (2016).
20. H. B. Lassen, E. J. R. Kelleher, L. Iliushyn, T. J. Booth, P. Bøggild, P. U. Jepsen, Terahertz s-SNOM reveals nanoscale conductivity of graphene. arXiv:2310.07479 [physics.optics] (2023).
21. Y. Kurman, R. Dahan, H. H. Sheinfux, K. Wang, M. Yannai, Y. Adiv, O. Reinhardt, L. H. G. Tizei, S. Y. Woo, J. Li, J. H. Edgar, M. Kociak, F. H. L. Koppens, I. Kaminer, Spatiotemporal imaging of 2D polariton wave packet dynamics using free electrons. *Science* **372**, 1181–1186 (2021).
22. E. Yoxall, M. Schnell, A. Y. Nikitin, O. Txoperena, A. Woessner, M. B. Lundeberg, F. Casanova, L. E. Hueso, F. H. L. Koppens, R. Hillenbrand, Direct observation of ultraslow hyperbolic polariton propagation with negative phase velocity. *Nat. Photonics* **9**, 674–678 (2015).
23. O. Mitrofanov, W. Yu, R. J. Thompson, Y. Jiang, Z. J. Greenberg, J. Palmer, I. Brener, W. Pan, C. Berger, W. A. de Heer, Z. Jiang, Terahertz near-field imaging of surface plasmon waves in graphene structures. *Solid State Commun.* **224**, 47–52 (2015).
24. T. Feurer, J. C. Vaughan, K. A. Nelson, Spatiotemporal coherent control of lattice vibrational waves. *Science* **299**, 374–377 (2003).
25. I. Torre, L. V. de Castro, B. V. Duppen, D. B. Ruiz, F. M. Peeters, F. H. L. Koppens, M. Polini, Acoustic plasmons at the crossover between the collisionless and hydrodynamic regimes in two-dimensional electron liquids. *Phys Rev. B* **99**, 144307 (2019).
26. D. N. Basov, M. M. Fogler, A. Lanzara, F. Wang, Y. Zhang, Colloquium: Graphene spectroscopy. *Rev. Mod. Phys.* **86**, 959–994 (2014).
27. Q. Xing, C. Song, C. Wang, Y. Xie, S. Huang, F. Wang, Y. Lei, X. Yuan, C. Zhang, L. Mu, Y. Huang, F. Xiu, H. Yan, Tunable terahertz plasmons in graphite thin films. *Phys. Rev. Lett.* **126**, 147401 (2021).
28. S. D. Sarma, Q. Li, Intrinsic plasmons in two-dimensional Dirac materials. *Phys. Rev. B* **87**, 235418 (2013).
29. T. Sohier, M. Calandra, C.-H. Park, N. Bonini, N. Marzari, F. Mauri, Phonon-limited resistivity of graphene by first-principles calculations: Electron-phonon interactions, strain-induced gauge field, and Boltzmann equation. *Phys Rev. B* **90**, 125414 (2014).
30. C. A. Kukkonen, P. F. Maldague, Electron-hole scattering and the electrical resistivity of the semimetal TiS_2. *Phys. Rev. Lett.* **37**, 782–785 (1976).
31. Y. Nam, D.-K. Ki, D. Soler-Delgado, A. F. Morpurgo, Electron–hole collision limited transport in charge-neutral bilayer graphene. *Nat. Phys.* **13**, 1207–1214 (2017).
32. C. Tan, D. Y. H. Ho, L. Wang, J. I. A. Li, I. Yudhistira, D. A. Rhodes, T. Taniguchi, K. Watanabe, K. Shepard, P. L. McEuen, C. R. Dean, S. Adam, J. Hone, Dissipation-enabled hydrodynamic conductivity in a tunable bandgap semiconductor. *Sci. Adv.* **8**, eabi8481 (2022).
33. L. W. Davies, Electron-hole scattering at high injection-levels in germanium. *Nature* **194**, 762–763 (1962).
34. R. A. Höpfel, J. Shah, P. A. Wolff, A. C. Gossard, Electron-hole scattering in GaAs quantum wells. *Phys. Rev. B* **37**, 6941–6954 (1988).
35. D. Svintsov, Hydrodynamic-to-ballistic crossover in Dirac materials. *Phys. Rev. B* **97**, 121405 (2018).
36. Z. Sun, D. N. Basov, M. M. Fogler, Universal linear and nonlinear electrodynamics of a Dirac fluid. *Proc. Natl. Acad. Sci. U.S.A.* **115**, 3285–3289 (2018).
37. A. Principi, G. Vignale, M. Carrega, M. Polini, Bulk and shear viscosities of the two-dimensional electron liquid in a doped graphene sheet. *Phys. Rev. B* **93**, 125410 (2016).
38. G. X. Ni, L. Wang, M. D. Goldflam, M. Wagner, Z. Fei, A. S. McLeod, M. K. Liu, F. Keilmann, B. Özyilmaz, A. H. C. Neto, J. Hone, M. M. Fogler, D. N. Basov, Ultrafast optical switching of infrared plasmon polaritons in high-mobility graphene. *Nat. Photonics* **10**, 244–247 (2016).
39. H. Moussa, G. Xu, S. Yin, E. Galiffi, Y. Ra'di, A. Alù, Observation of temporal reflection and broadband frequency translation at photonic time interfaces. *Nat. Phys.* **19**, 863–868 (2023).
40. X. Zhang, Q. Yan, W. Ma, T. Zhang, X. Yang, X. Zhang, P. Li, Ultrafast anisotropic dynamics of hyperbolic nanolight pulse propagation. *Sci. Adv.* **9**, eadi4407 (2023).
41. Z. Yao, S. Xu, D. Hu, X. Chen, Q. Dai, M. Liu, Nanoimaging and nanospectroscopy of polaritons with time resolved *s*-SNOM. *Adv. Opt. Mater.* **8**, 1901042 (2020).
42. A. J. Sternbach, S. H. Chae, S. Latini, A. A. Rikhter, Y. Shao, B. Li, D. Rhodes, B. Kim, P. J. Schuck, X. Xu, X.-Y. Zhu, R. D. Averitt, J. Hone, M. M. Fogler, A. Rubio, D. N. Basov, Programmable hyperbolic polaritons in van der Waals semiconductors. *Science* **371**, 617–620 (2021).
43. N. S. Stoyanov, D. W. Ward, T. Feurer, K. A. Nelson, Terahertz polariton propagation in patterned materials. *Nat. Mater.* **1**, 95–98 (2002).
44. Q. Zhang, M. Lou, X. Li, J. L. Reno, W. Pan, J. D. Watson, M. J. Manfra, J. Kono, Collective non-perturbative coupling of 2D electrons with high-quality-factor terahertz cavity photons. *Nat. Phys.* **12**, 1005–1011 (2016).
45. X. Li, M. Bamba, Q. Zhang, S. Fallahi, G. C. Gardner, W. Gao, M. Lou, K. Yoshioka, M. J. Manfra, J. Kono, Vacuum Bloch–Siegert shift in Landau polaritons with ultra-high cooperativity. *Nat. Photonics* **12**, 324–329 (2018).
46. O. Mitrofanov, I. Khromova, T. Siday, R. J. Thompson, A. N. Ponomarev, I. Brener, J. L. Reno, Near-field spectroscopy and imaging of subwavelength plasmonic terahertz resonators. *IEEE Trans. Terahertz Sci. Technol.* **6**, 382–388 (2016).
47. M. E. Berkowitz, B. S. Y. Kim, G. Ni, A. S. McLeod, C. F. B. Lo, Z. Sun, G. Gu, K. Watanabe, T. Taniguchi, A. J. Millis, J. C. Hone, M. M. Fogler, R. D. Averitt, D. N. Basov, Hyperbolic Cooper-pair polaritons in Planar graphene/cuprate plasmonic cavities. *Nano Lett.* **21**, 308–316 (2020).
48. Z. Sun, M. M. Fogler, D. N. Basov, A. J. Millis, Collective modes and terahertz near-field response of superconductors. *Phys. Rev. Res.* **2**, 023413 (2020).
49. M. Dapolito, M. Tsuneto, W. Zheng, L. Wehmeier, S. Xu, X. Chen, J. Sun, Z. Du, Y. Shao, R. Jing, S. Zhang, A. Bercher, Y. Dong, D. Halbertal, V. Ravindran, Z. Zhou, M. Petrovic, A. Gozar, G. L. Carr, Q. Li, A. B. Kuzmenko, M. M. Fogler, D. N. Basov, X. Du, M. Liu, Infrared nano-imaging of Dirac magnetoexcitons in graphene. *Nat. Nanotechnol.* **18**, 1516 (2023).
50. X. Huang, A. Lucas, Electron-phonon hydrodynamics. *Phys. Rev. B* **103**, 155128 (2021).
51. F. H. L. Koppens, T. Mueller, P. Avouris, A. C. Ferrari, M. S. Vitiello, M. Polini, Photodetectors based on graphene, other two-dimensional materials and hybrid systems. *Nat. Nanotechnol.* **9**, 780–793 (2014).
52. M. B. Lundeberg, Y. Gao, R. Asgari, C. Tan, B. V. Duppen, M. Autore, P. Alonso-González, A. Woessner, K. Watanabe, T. Taniguchi, R. Hillenbrand, J. Hone, M. Polini, F. H. L. Koppens, Tuning quantum nonlocal effects in graphene plasmonics. *Science* **357**, 187–191 (2017).
53. D. B. Ruiz, N. C. H. Hesp, H. H. Sheinfux, C. R. Marimón, C. M. Maissen, A. Principi, R. Asgari, T. Taniguchi, K. Watanabe, M. Polini, R. Hillenbrand, I. Torre, F. H. L. Koppens, Experimental signatures of the transition from acoustic plasmon to electronic sound in graphene. *Sci. Adv.* **9**, eadi0415 (2023).
54. C. R. Dean, A. F. Young, I. Meric, C. Lee, L. Wang, S. Sorgenfrei, K. Watanabe, T. Taniguchi, P. Kim, K. L. Shepard, J. Hone, Boron nitride substrates for high-quality graphene electronics. *Nat. Nanotechnol.* **5**, 722–726 (2010).
55. S. Xu, A. S. McLeod, X. Chen, D. J. Rizzo, B. S. Jessen, Z. Yao, Z. Wang, Z. Sun, S. Shabani, A. N. Pasupathy, A. J. Millis, C. R. Dean, J. C. Hone, M. Liu, D. N. Basov, Deep learning analysis of polaritonic wave images. *ACS Nano* **15**, 18182–18191 (2021).
56. M. Müller, L. Fritz, S. Sachdev, Quantum-critical relativistic magnetotransport in graphene. *Phys. Rev. B* **78**, 115406 (2008).
57. B. Wunsch, T. Stauber, F. Sols, F. Guinea, Dynamical polarization of graphene at finite doping. *New J. Phys.* **8**, 318 (2006).
58. E. H. Hwang, S. D. Sarma, Dielectric function, screening, and plasmons in two-dimensional graphene. *Phys. Rev. B* **75**, 205418 (2007).
59. T. Li, J. Ingham, H. D. Scammell, Artificial graphene: Unconventional superconductivity in a honeycomb superlattice. *Phys. Rev. Res.* **2**, 043155 (2020).
60. A. B. Kuzmenko, E. van Heumen, F. Carbone, D. van der Marel, Universal optical conductance of graphite. *Phys. Rev. Lett.* **100**, 117401 (2008).
61. S. Dai, Q. Ma, Y. Yang, J. Rosenfeld, M. D. Goldflam, A. McLeod, Z. Sun, T. I. Andersen, Z. Fei, M. Liu, Y. Shao, K. Watanabe, T. Taniguchi, M. Thiemens, F. Keilmann, P. Jarillo-Herrero, M. M. Fogler, D. N. Basov, Efficiency of launching highly confined polaritons by infrared light incident on a hyperbolic material. *Nano Lett.* **17**, 5285–5290 (2017).

Acknowledgments

Funding: Research on electronic interactions in graphene is supported by DOE-BES DE-SC0018426. The development of spacetime metrology is supported as part of Programmable Quantum Materials, an Energy Frontier Research Center funded by the US Department of Energy (DOE), Office of Science, Basic Energy Sciences (BES), under award DE-SC0019443. D.N.B. is the Moore investigator in quantum Materials EPIQS GBMF9455 and Vannevar Bush Faculty Fellow ONR-VB: N00014-19-1-2630. S.X., R.A.V., R.J., M.L., and D.N.B. acknowledge support for THz-SNOM development from the US Department of Energy (DOE), Office of Science, National Quantum Information Science Research Centers, Co-design Center for Quantum Advantage (contract no. DE-SC0012704). M.L. acknowledges support from the NSF Faculty Early Career Development Program under grant no. DMR - 2045425. **Author contributions:** D.N.B. conceived of the study. S.X. recorded the near-field data with assistance from R.A.V., R.J., A.J.S., and S.Z.; Y.L. prepared the samples, with guidance from J.H. and C.R.D.; S.X. performed theoretical calculations and numerical simulations, with assistance from R.J., J.I., R.Q., A.J.M., and M.M.F.; S.X. analyzed the data with assistance from R.A.V., R.J., A.J.S, S.Z., M.D., J.W.M., M.Y., A.J.M., M.M.F., and M.L.; S.X. and D.N.B. wrote the manuscript with input from all the coauthors. **Competing interests:** The authors declare that they have no competing interests. **Data and materials availability:** All data needed to evaluate the conclusions in the paper are present in the paper and/or the Supplementary Materials.

Submitted 7 February 2024
Accepted 17 September 2024
Published 23 October 2024
10.1126/sciadv.ado5553